

New Strategies for Direct Methane-to-Methanol Conversion from Active Learning Exploration of 16 Million Catalysts

Aditya Nandy^{1,2}, Chenru Duan^{1,2}, Conrad Goffinet¹, and Heather J. Kulik^{1,*}

¹*Department of Chemical Engineering, Massachusetts Institute of Technology, Cambridge, MA, 02139*

²*Department of Chemistry, Massachusetts Institute of Technology, Cambridge, MA, 02139*

AUTHOR INFORMATION

Corresponding Author

*email: hjkulik@mit.edu, phone: 617-253-4584

ABSTRACT: Despite decades of effort, no earth abundant homogeneous catalysts have been discovered that can selectively oxidize methane to methanol. We exploit active learning to simultaneously optimize methane activation and methanol release calculated with machine learning (ML)-accelerated density functional theory (DFT) in a space of 16M candidate catalysts with novel macrocycles. By constructing these macrocycles from fragments inspired by synthesized compounds, we ensure synthetic realism in our computational search. Our large-scale search reveals that low spin Fe(II) compounds paired with strong field (e.g. P or S-coordinating) ligands have the best energetic tradeoff between hydrogen atom transfer (HAT) and methanol release. This observation is distinct from prior efforts that have focused on high spin Fe(II) with weak field ligands. By decoupling equatorial and axial ligand effects, we determine that negatively charged axial ligands are critical for more rapid release of methanol and, higher valency metals (i.e., M(III) vs M(II)) are unlikely to be suitable for methanol release. With full characterization of barrier heights, we confirmed that optimizing for HAT did not lead to large oxo formation barriers. Energetic span analysis revealed designs for an intermediate spin Mn(II) catalyst and a low spin Fe(II) catalyst that would lead to good turnover frequencies. This active learning approach is expected to be beneficial for search of large catalyst spaces where no prior designs have been identified and where linear scaling relationships between reaction energies or barriers may be limited or unknown.

1. Introduction

Direct methane-to-methanol conversion with high selectivity remains a challenge¹ in unlocking natural gas as a feedstock.² Catalysts that can readily convert methane into methanol must be potent enough to activate the strong C-H bonds of methane but also release methanol to facilitate catalyst turnover and avoid catalyst poisoning or methanol overoxidation.^{3,4} Thus, the design of the optimal catalysts for methane-to-methanol or similarly challenging reactions requires balancing inherent tradeoffs between activity, selectivity, and stability, motivating an exhaustive search over chemical space.⁵ Enzymes with mononuclear Fe active sites (e.g. TauD⁶⁻⁸ or P450^{9,10}) have demonstrated the capability to perform selective partial oxidation of substrates with strong C-H bonds, including methane. These enzymes have thus motivated the design of ligands¹¹⁻¹⁴ for synthetic systems, including both homogeneous¹⁵⁻¹⁸ and heterogeneous¹⁹⁻²² catalysts. Nevertheless, to date no Earth abundant molecular catalyst has been identified that can meet all criteria.

Compounding the challenges of the need to search a large space, high-valent metal-oxo moieties that are frequently invoked for C-H bond activation²³ on transition metal complexes^{14, 24-28}, heterogeneous catalysts²⁹⁻³⁵, or enzymes^{6, 7, 10} are challenging to isolate and characterize experimentally³⁶⁻⁴¹. Instead, first-principles computation with density functional theory (DFT) has filled this gap⁴²⁻⁴⁶ in understanding the electronic structure⁴⁷⁻⁵⁰ needed for C-H bond activation. First-principles modeling has revealed the role of spin state in reactivity⁵¹⁻⁵⁵, and revealed the importance of multi-state reactivity⁵⁶⁻⁵⁹ that is difficult to study experimentally.⁶⁰ To reduce the computational cost of catalyst screening needed to explore a large chemical space, it is appealing to extend to homogeneous catalysis^{61, 62} the linear free energy relationships (LFERs)^{29, 63-67} between thermodynamic steps or Brønsted-Evans-Polanyi (BEPs)⁶⁸⁻⁷¹ linear

scaling relationships between barrier heights and reaction energies. Nevertheless, in open shell transition metal catalysis, the nature of the LFERs or BEPs are rarely known beforehand⁷². These relationships are also easily disrupted by changes in metal-local structure⁷³⁻⁷⁵ or spin state^{24, 76}. Although these disruptions in thermodynamic or kinetic scaling increase computational cost by requiring full characterization of the catalytic cycle, they simultaneously provide the opportunity for overcoming kinetic or thermodynamic limitations observed in catalysts that obey these scaling relations, potentially providing paths to overcome challenges in direct methane-to-methanol conversion.

Thus far, an Edisonian approach for catalyst design has been unsuccessful in identifying effective molecular catalysts for direct methane-to-methanol conversion, in part because the variations in chemistry that can be searched in one single study are fairly limited (e.g., to Hammett tuning^{26, 77, 78}). As an alternative approach, the absence of universal scaling relations between intermediate energetics provides an opportunity for non-linear machine learning (ML) models that can be used over a larger space. Rather than relying on linear relationships between quantities or small variations in chemistry, ML models can be trained to directly predict catalyst reactivity on the basis of chemical composition and applied to thousands of compounds.⁷⁹ In recent years, this strategy has reduced the time to property prediction to seconds, which would otherwise take days using DFT, and has led to accurate predictions of reaction energetics⁸⁰⁻⁸³, redox and ionization potentials⁸⁴⁻⁸⁷, and frontier orbital energetics^{88, 89} that pave the way for catalyst discovery over large chemical spaces. Importantly, they have demonstrated the limits of conventional descriptor-based screening, highlighting where quantities like the frontier orbital energies of reactive intermediates are poor predictors of reaction energies.⁸⁰

A key trade-off for the machine learning approach is that data must be acquired to make the models predictive. When aiming to search a large space of catalysts or materials, active learning⁹⁰⁻⁹⁴ is instead preferred as a way to acquire data^{95, 96} where models are most uncertain.⁹⁷ ⁹⁸ For example, efficient global optimization^{99, 100} (EGO) was employed to search a space of 2.8 M redox flow couples⁸⁴ to reveal design principles in weeks instead of decades. It is thus attractive to exploit similar approaches for search of C-H activation catalysts, given no mid-row 3d transition metal complexes can efficiently convert methane into methanol.⁶⁹

In this work, we construct a 16M compound space of realistic Mn and Fe catalysts with novel tetradentate macrocycles and coordinating axial ligands. We demonstrate that our active learning approach enables the discovery of optimal catalysts in the design space where strong thermodynamic or kinetic scaling relations do not hold. We decouple the roles of axial and equatorial ligands on tuning reaction energetics and determine that Hammett tuning on catalysts has a modest effect relative to optimal macrocycle design or axial ligand selection. These discovered lead compounds provide alternative designs with novel spin state and ligand chemistry in comparison to prior known best-in-class catalysts.

2. Reaction Mechanism.

We calculate the reaction energies for the radical rebound mechanism¹⁰¹ for methane-to-methanol conversion on mononuclear Mn and Fe catalysts. For these catalysts, we consider two resting state oxidation states, M(II) and M(III), in their corresponding spin states (Supporting Information Table S1). We do not study Cr and Co catalysts because Cr catalysts form terminal metal-oxo moieties that are too stable and cannot activate C-H bonds^{24, 102} while Co metal-oxo intermediates are rarely stable (i.e., are past the oxo wall).¹⁰³ From a resting state structure (**1**), we form a high valent terminal metal-oxo (**2**) upon two-electron metal oxidation by nitrous oxide

(Figure 1). An alternate oxidant choice (i.e. triplet O₂) will rigidly shift reaction energetics but does not affect relative energetics (Supporting Information Table S2). We compute the oxo formation energy ($\Delta E(\text{oxo})$) as:

$$\Delta E(\text{oxo}) = E(2) + E(\text{N}_2) - E(1) - E(\text{N}_2\text{O})$$

Upon oxo formation, the metal formal oxidation state changes from M(II/III) to M(IV/V). The high valent M(IV/V)=O intermediate then undergoes hydrogen atom transfer (HAT) from a methane substrate to form a M(III/IV)-OH intermediate (**3**), leaving a methyl radical (Figure 1). We compute the reaction energy for the HAT step ($\Delta E(\text{HAT})$) as:

$$\Delta E(\text{HAT}) = E(3) + E(\cdot\text{CH}_3) - E(2) - E(\text{CH}_4)$$

Following HAT, the methyl radical rebounds with the M(III/IV)-OH intermediate to form a metal-bound methanol intermediate (**4**, Figure 1). We compute the $\Delta E(\text{rebound})$ step as:

$$\Delta E(\text{rebound}) = E(4) - E(3) - E(\cdot\text{CH}_3)$$

The catalyst then returns to its resting state (1) upon methanol release ($\Delta E(\text{release})$):

$$\Delta E(\text{release}) = E(1) + E(\text{CH}_3\text{OH}) - E(4)$$

Although both oxo formation^{73, 104} and hydrogen atom transfer^{105, 106} can be turnover determining, methanol release is believed to be a universal thermodynamic sink in the radical rebound mechanism.^{24, 102}

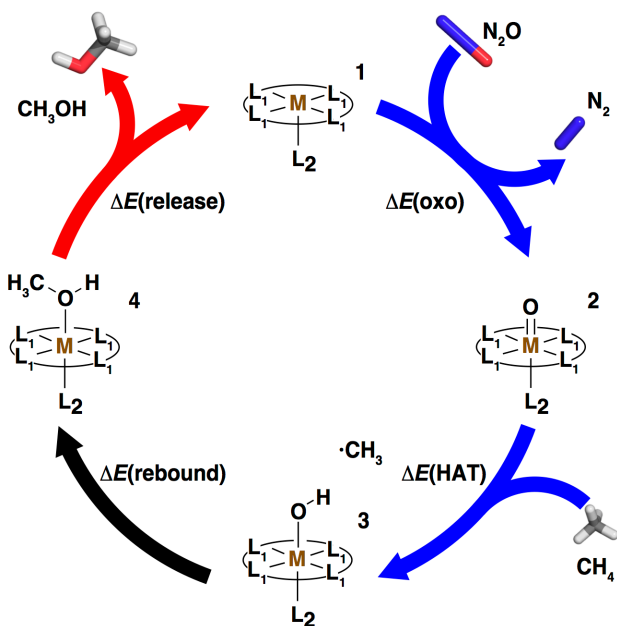


Figure 1. The radical rebound mechanism for partial oxidation of methane to methanol. The cycle proceeds clockwise from the resting state (**1**) in oxidation state $n = \text{II/III}$, to the metal-oxo intermediate (**2**) formed by two-electron oxidation with N_2O , followed by hydrogen atom transfer to form a metal-hydroxo intermediate (**3**), and rebound to form a metal-bound methanol intermediate (**4**). A representative catalyst is shown, with the metal (M) shown in brown, corresponding to Mn and Fe in this work. All catalysts have a tetradentate equatorial ligand (L_1) and a monodentate axial ligand (L_2). We color the arrows of steps that have been observed to be turnover determining, with potential turnover determining transition states in blue and the turnover determining intermediate in red.

3. Design Space and Objectives.

Molecular complexes that have been studied for C–H activation typically consist of Fe(II) centers coordinated by nitrogen atoms in analogy to enzymes^{11, 107, 108}. This means many chemical environments, such as those with O, P, and S-coordinating atoms, have not been thoroughly examined for C–H activation, motivating their inclusion in a wider search. To create an expanded space of macrocycles that are likely to be synthetically accessible, we design realistic ligands by recombining fragments of known ligands into new tetradentate macrocycles, ultimately producing spaces as large as 16 M catalysts. From this space, we aim to discover

ligand chemistry that optimally tunes catalyst energetics to reach the “utopia point”¹⁰⁹ where a catalyst will simultaneously activate methane and release methanol.

As an example of our fragment-based approach, the pyrrole subunits that comprise a porphyrin and the dimethylamine subunits that comprise a cyclam can be combined to produce new macrocycles (Figure 2). We also include $3p$ equivalents of more well studied $2p$ fragments (e.g., P-coordinating phosphole in analogy to N-coordinating pyrrole, Figure 2). Many of these fragments have been part of synthesized macrocycles^{110, 111} but not necessarily in those that have been studied for C–H activation. In select cases, fragments may favor multiple charge states (e.g., pyrrole and phosphole), and in those cases we consider all possibilities to construct macrocycles (Supporting Information Figures S1 and S2). We join fragments together with compatible bridge atoms that determine the macrocycle ring size and aromaticity (Supporting Information Tables S3 and S4). These combinations result in 16,986 candidate tetradentate macrocycles of varying in coordination atom identities, size, ring size, charge, and aromaticity (Supporting Information Table S4 and Figure S3).

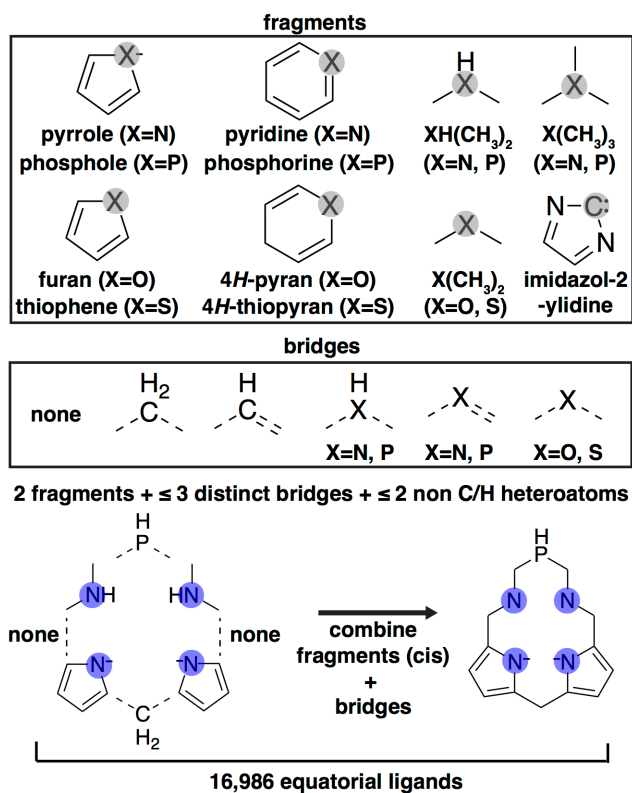


Figure 2. 15 fragments (top) and 9 bridges (middle) that are used to construct tetradentate macrocycles in transition metal complexes for light alkane oxidation. All metal-coordinating atoms are highlighted by gray circles, and X is used to indicate the possibility of multiple metal-coordinating element types. Two fragment types in cis orientation are combined with up to three distinct bridges to construct a macrocycle. (bottom) An example macrocycle is shown that is constructed from two dimethylamine fragments and two pyrrole fragments joined via one phosphorus bridge, one methylene bridge, and two bridges with no atoms.

Our ligand design strategy reproduces existing chemistry such as porphyrins, corroles, and cyclams but also extends beyond to other candidate macrocycles (Supporting Information Figure S4). Quantitatively, comparison of our database to tetradentate ligands that exist in the Cambridge Structural Database¹¹² (CSD), demonstrates that our candidate ligand space reproduces existing local chemical environments and introduces new environments that are yet to be reported in the experimental literature (Supporting Information Figure S5). We combine these tetradentate macrocycles with 8 possible neutral and anionic axial ligands and 9 metal oxidation-

and spin- state combinations (i.e., M(II/III) where M = Mn or Fe in LS, IS, and HS states) to make an initial design space of over 1.2M candidate complexes (Supporting Information Figure S6). The addition of functional groups to these macrocycles later led to a space of 16 M candidate complexes. For complexes that have distinct connectivity but are duplicates in revised autocorrelation⁸⁵ (RAC) descriptor space (i.e., are isomers), we systematically retain one case, after controlled studies that demonstrated only minor differences in catalyst thermodynamics between the two isomers (Supporting Information Figure S7).

We use EGO¹¹³ with a 2D expected improvement (2D-EI) criterion¹⁰⁰ to simultaneously optimize $\Delta E(\text{HAT})$ and $\Delta E(\text{release})$ because a catalyst must simultaneously activate methane and desorb methanol to prevent overoxidation of methanol.^{3, 5} We also selected HAT and release to simultaneously optimize because moderate scaling between $\Delta E(\text{oxo})$ and $\Delta E(\text{HAT})$ within a single metal/oxidation state suggests²⁴ greater opportunities to independently optimize HAT and release than HAT and oxo formation. The ML-model predicted $\Delta E(\text{HAT})$ and $\Delta E(\text{release})$ values for a new complex, x , are determined as:

$$\begin{matrix} \Delta E(\text{HAT})(x) \\ \Delta E(\text{release})(x) \end{matrix} \approx \text{N} \left(\begin{bmatrix} \hat{\mu}_{\Delta E(\text{HAT})} \\ \hat{\mu}_{\Delta E(\text{release})} \end{bmatrix}, \begin{bmatrix} \hat{\sigma}_{\Delta E(\text{HAT})}^2 & 0 \\ 0 & \hat{\sigma}_{\Delta E(\text{release})}^2 \end{bmatrix} \right)$$

where $\hat{\mu}_{\Delta E(\text{HAT})}$ and $\hat{\mu}_{\Delta E(\text{release})}$ are the ML-model predicted mean values and $\hat{\sigma}_{\Delta E(\text{HAT})}^2$ and $\hat{\sigma}_{\Delta E(\text{release})}^2$ are the effective variances from the model uncertainty.¹⁰⁰ The protocol we employ largely follows prior work⁸⁴, where we use ANN models with calibrated latent space uncertainty metric^{84, 97} as our surrogate models, and we employ k -medoids sampling at each generation to generate new DFT data and retrain our models (Supporting Information Figure S8 and Text S1).⁸⁴

4. Results and Discussion.

4.1 Design Outcomes in Initial Macrocyclic Space.

To start our exploration of the catalyst space, we performed k -medoids sampling over the 1.2M compound design space to generate an initial set of reaction energies for ML model training (Supporting Information Figure S9). We then trained independent ANN models to predict $\Delta E(\text{HAT})$ and $\Delta E(\text{release})$ (Supporting Information Figure S10). For the first generation (i.e., generation 0), we collected 516 pairs of $\Delta E(\text{HAT})$ and $\Delta E(\text{release})$ reaction energies and used them to train ANNs with RACs as input features (Supporting Information Tables S5-S7). Although efficient global optimization is typically carried out with Gaussian process (GP) models, we selected independent ANNs because they have superior performance on the generation 0 test data (Supporting Information Table S7 and Figure S11). As in prior work⁸⁴, we used the 10-nearest-neighbor ANN latent space distances⁹⁷ to training data as an uncertainty quantification (UQ) metric (Supporting Information Figure S12). The latent space distance provides an intuitive measure of UQ and brings to an ANN-based approach the benefit that the GPs normally have of including built-in uncertainty.

We then applied the trained ANN models to predict reaction energies for the full 1.2M compound design space and select new catalysts for DFT characterization based on their 2D-EI scores (Supporting Information Table S8). This allows us to improve ANN model performance at the Pareto front while discovering new Pareto-optimal catalysts. At each generation, we selected the top 10,000 catalysts by their $E[\text{I}]$ scores and performed k -medoids sampling to initiate 400 representative metal-oxo DFT calculations for model retraining in subsequent generations (Supporting Information Table S9 and Figures S13 and S14). To quantify model improvement by generation, we use lookahead errors⁸⁴ that quantify the ability of models to

predict properties for subsequent generations. Over three full generations of 2D-EI, $\Delta E(\text{HAT})$ lookahead errors reduce threefold (i.e., from 15 to 5 kcal/mol), and $\Delta E(\text{release})$ lookahead errors are reduced twofold (i.e., from 8 to 4 kcal/mol). Model errors on set aside test data at each generation also improve to a lesser degree (Figure 3 and Supporting Information Figures S15 and S16). We thus stopped the search for Pareto optimal catalysts after three generations, as lookahead errors approach test set errors by this point and average $E[\text{I}]$ scores decrease markedly (Figure 3 and Supporting Information Figure S17).

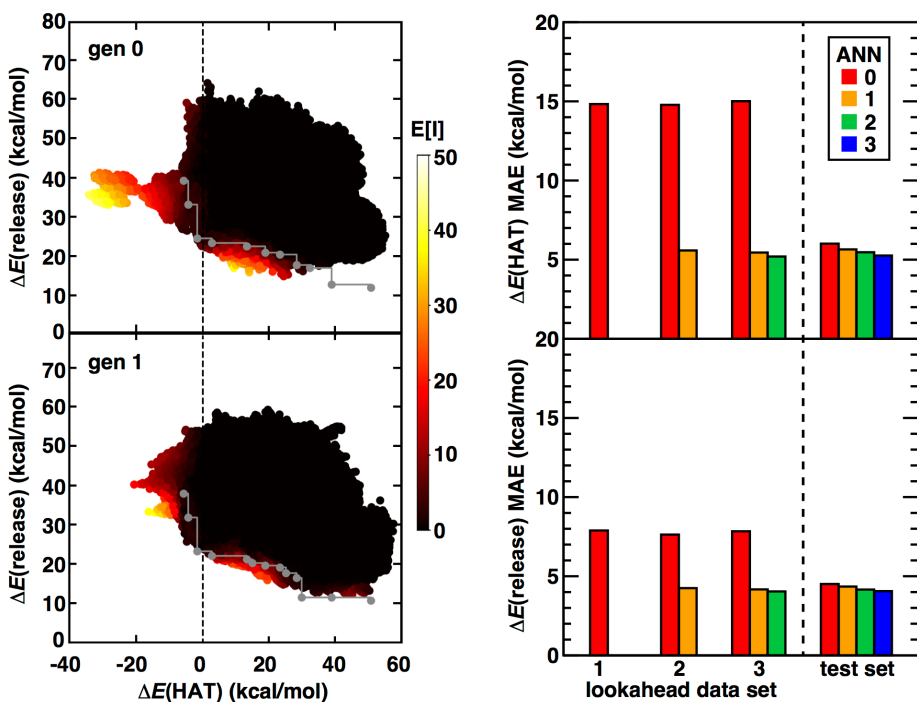


Figure 3. (left) $E[\text{I}]$ over the initial ligand space as predicted by ANN models during generation 0 (top) and generation 1 (bottom). The Pareto front after each generation is shown in gray. (right) Lookahead and test set mean absolute errors (MAEs) for $\Delta E(\text{HAT})$ (top, in kcal/mol) and $\Delta E(\text{release})$ (bottom) for the two single task ANNs. Each bar is colored by the generation at which it is trained, as indicated in the top inset. Lookahead MAEs are reported on data sets (1–3, as indicated on axis) generated in each relevant subsequent generation. The MAEs on a test set representative for each generation are reported.

Studies of bio-inspired Fe(II) compounds have typically targeted C–H bond reactivity for

high-spin (HS) Fe(II) because most enzymes capable of C–H activation are believed to be HS Fe(II) stabilized by weak field N- and O-coordinating species. At odds with these expectations, we observe low-spin (LS) Fe(II) compounds to have the best tradeoff between $\Delta E(\text{HAT})$ and $\Delta E(\text{release})$ on the Pareto front, having both the most favorable HAT thermodynamics and not binding methanol too tightly (Figure 4). This observation was made possible by the EGO exploration because our initial sampling of the design space had instead primarily favored intermediate spin (IS) Mn(II) compounds (Figure 4 and Supporting Information Figures S18 and S19). After three generations of EGO, only a single IS Mn(II) catalyst is Pareto optimal and LS Fe(II) catalysts with weak field oxygen coordinating (e.g. dimethylether, 4*H*-pyran, and furan) fragments occupy the majority of the Pareto front (Figure 4 and Supporting Information Table S10). The relative position of a catalyst on the Pareto front is governed by the equatorial ligand field strength: stronger ligand fields with donating equatorial ligands have favorable $\Delta E(\text{release})$ and unfavorable $\Delta E(\text{HAT})$. The compounds that have the most favorable HAT thermodynamics at the cost of binding methanol more tightly primarily contain oxygen-coordinating macrocycles, whereas those that release methanol more readily but do not favor HAT contain 3*p*-coordinating macrocycles (Figure 4 and Supporting Information Figure S18). Over this 1.2M initial design space, EGO reveals ligands that have been understudied (e.g. 3*p*-coordinating ligands) combined with LS Fe(II) will lead to ground state complexes that demonstrate a good balance between $\Delta E(\text{HAT})$ and $\Delta E(\text{release})$.

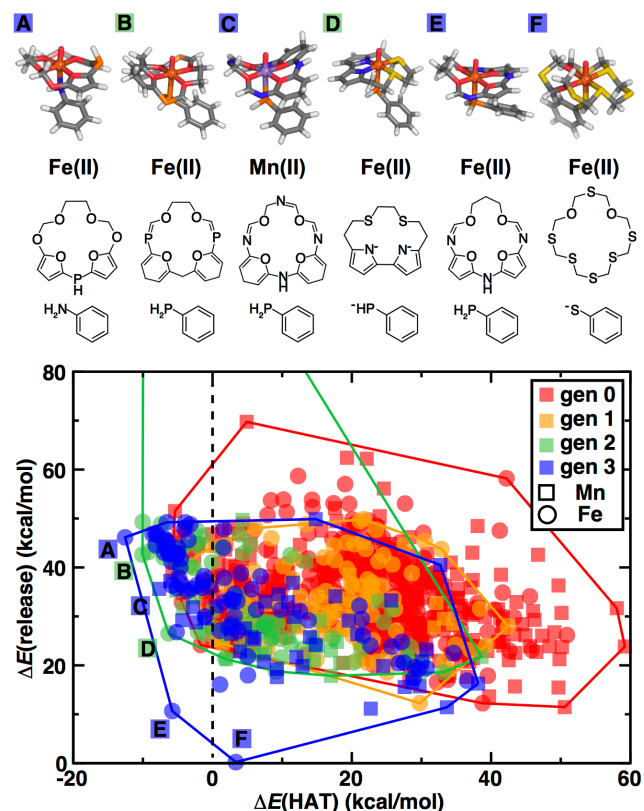


Figure 4. (top) Pareto optimal compounds from the initial ligand space simulated during three generations of the design algorithm in the ball and stick representation, with Fe in brown, Mn in purple, C in gray, N in blue, O in red, P in orange, and S in yellow. (middle) fragments that make up Pareto optimal compounds in the initial ligand space. (bottom) Compounds simulated during three generations of the design algorithm, colored by generation and with unique symbols for each metal center (as indicated in inset legend). The range of values sampled in each generation is indicated by a convex hull. For generation 2, four outlier points that expand the convex hull are truncated from the plot. A final Pareto front is indicated by letters A-F.

4.2 Exploring Hammett Tuning Effects on Macrocycles.

A frequently pursued synthetic approach to fine tuning catalyst reaction energetics is to functionalize macrocycles with electron withdrawing or donating groups. To evaluate the utility of this strategy, we performed controlled studies on functionalized porphyrins, which suggested the possibility to tune macrocycle energetics by 5-15 kcal/mol (Supporting Information Figure S20). We thus functionalized the initial set of 1.2M macrocycles with common functional groups

used in Hammett tuning, which enlarges our catalyst space to 16M compounds (Figure 5). We functionalize all C–H bonds on bridges and C–H bonds on select fragments (Figure 5 and Supporting Information Figure S21). This approach reproduces well-studied macrocyclic ligands, such as phthalocyanine or tetraphenylporphyrin but also introduces new chemistry. There are differences in functional group effects for $\Delta E(\text{HAT})$ and $\Delta E(\text{release})$ on porphyrins, and so functionalization should alter both the relative positioning of catalysts on the Pareto front and change the identity of macrocycles on the Pareto front (Supporting Information Figures S22 and S23). Assuming this trend is general, it should also be possible to advance the Pareto front with functional group variation.

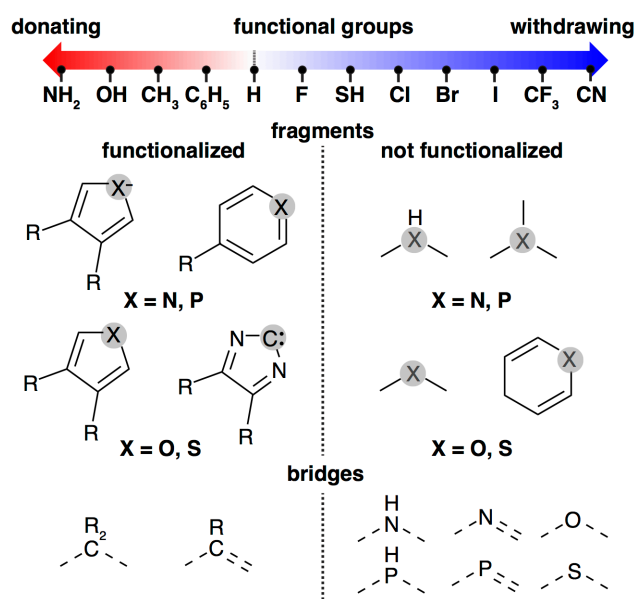


Figure 5. Functional groups used to perform Hammett tuning on macrocycles, ranging from electron donating groups to electron withdrawing groups. C–H bonds on select fragments and bridges (left) can be functionalized, while remaining fragments and bridges (right) are not considered for functionalization.

Although functional group addition tunes energetics by 5-15 kcal/mol on porphyrins, these functional groups are distant from the metal center on the molecular graph. The RAC

featurization we use has a default cutoff of correlating atoms only three bond paths (i.e., $d = 3$) apart. Thus, we revisited our models and examined the potential benefit of using higher depth ($d = 4$) RACs to ensure we adequately capture changes in functional groups (Supporting Information Figure S24). In combination with a revised feature set for model training, at the first generation with functional groups present (i.e., generation 4), we also sample the initial 16M compound space with k -medoids sampling to select 1,800 new data points (Supporting Information Tables S11 and S12 and Figure S25). The revised RACs representation improves model accuracy, reducing test set MAEs for both HAT and release to below 5 kcal/mol. This performance is superior to the best-performing models we obtained using the original RACs on this functionalized data (Supporting Information Figure S25).

To determine if we could extend the Pareto front, we carried out additional generations of EGO in the 16M compound functionalized macrocycle space. Since the functional groups expand our space 10-fold, we increased our selection of catalysts to the top 100,000 (i.e., as judged by $E[I]$ scores) over which we carried out k -medoids sampling (Supporting Information Figure S26). Over this expanded search in the 16M compound space, within three additional generations lookahead errors again reduce to test set errors and $E[I]$ values reduce significantly (Supporting Information Figures S27 and S28). For the final Pareto set, four out of the five Pareto-optimal catalysts are those obtained only after functionalization, while the one catalyst from the initial space contained no sites compatible with functionalization (Figures 4 and 6). The functional groups range from both electron donating (e.g. methyl and phenyl) to electron withdrawing (e.g. cyano and fluoro) on N or O coordinating equatorial ligands (Figure 6). Three out of the four Pareto optimal catalysts have functional groups on bridge C–H bonds, as opposed to on fragments, suggesting the greater importance of steric bulk in our functionalization strategy

in comparison to through-bond, electronic effects. We observe that functional groups do indeed shift catalysts to the Pareto front, as none of the initial versions of the functionalized macrocycles had unfunctionalized forms on the Pareto front optimization of the initial design space.

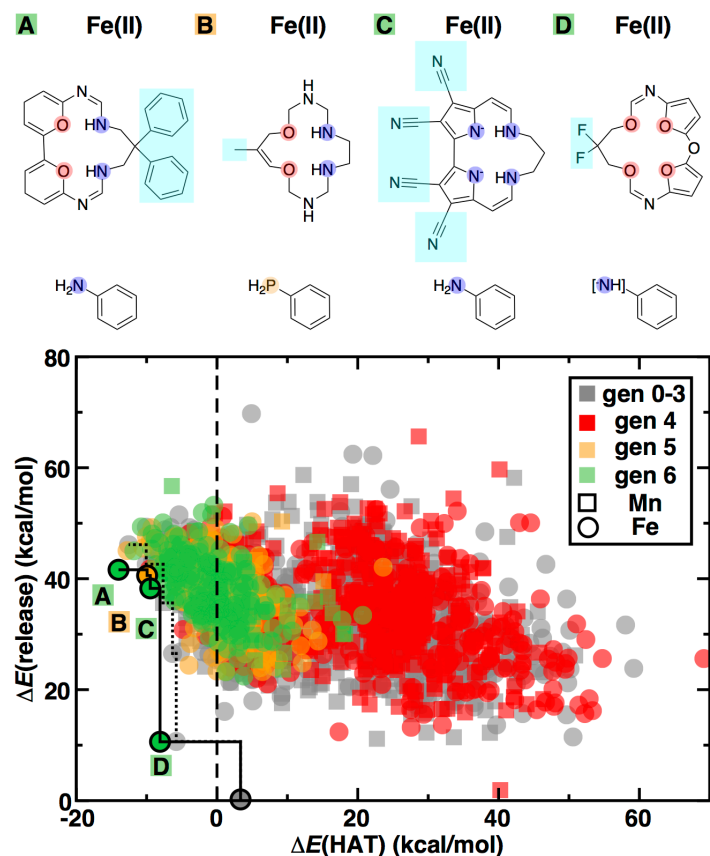


Figure 6. (top) Fragments that make up Pareto optimal compounds in the global functionalized ligand space simulated during three additional generations of the design algorithm after introducing functional groups. Functional groups are highlighted in cyan boxes, and metal coordinating atoms are indicated by translucent circles. (bottom) Compounds simulated during three additional generations of the design algorithm after introducing functional groups, colored by generation and with unique symbols for each metal center (as indicated in inset legend). The initial Pareto front, prior to the introduction of functional groups, is shown as a black dotted line. A final Pareto front is shown as a solid black line. New, functionalized compounds that reach the Pareto front are indicated by letters A-D. A black dashed line indicates a value of 0 for $\Delta E(\text{HAT})$.

4.3 Identifying Design Principles for Catalysts with Optimal Reaction Energetics.

Good catalysts for methane to methanol conversion should have equally favorable $\Delta E(\text{HAT})$ and $\Delta E(\text{release})$ while also being in their ground spin states. To identify the catalyst designs most likely to meet these criteria in our search space, we next applied relative energy cutoffs of $\Delta E(\text{HAT}) < 10$ kcal/mol and $\Delta E(\text{release}) < 30$ kcal/mol, as predicted by the generation 3 ML models. This reduces the theoretical space of catalysts to 30,095 compounds that represent 2.5% of the initial design space (Figure 7 and Supporting Information Figure S29). Small changes to the cutoff values will not alter conclusions about the compounds favored in this the space (Figure 7 and Supporting Information Figure S30). Examining this smaller set of compounds, we observe that the best catalysts have 15- or 16-membered rings (i.e., the same as corroles, porphyrins, and phthalocyanines), but the distribution of macrocycle ring sizes does not change after applying the energetic criteria (Supporting Information Table S10 and Figure S31). A clearer preference is established for the axial ligand within the cutoff zone: we observe a strong preference for anionic axial ligands with 3*p* coordinating atoms (Figure 7). The selection for these anionic axial ligands appears to have an overriding effect on energetics with respect to the equatorial macrocycle ligand chemistry (Figure 7).

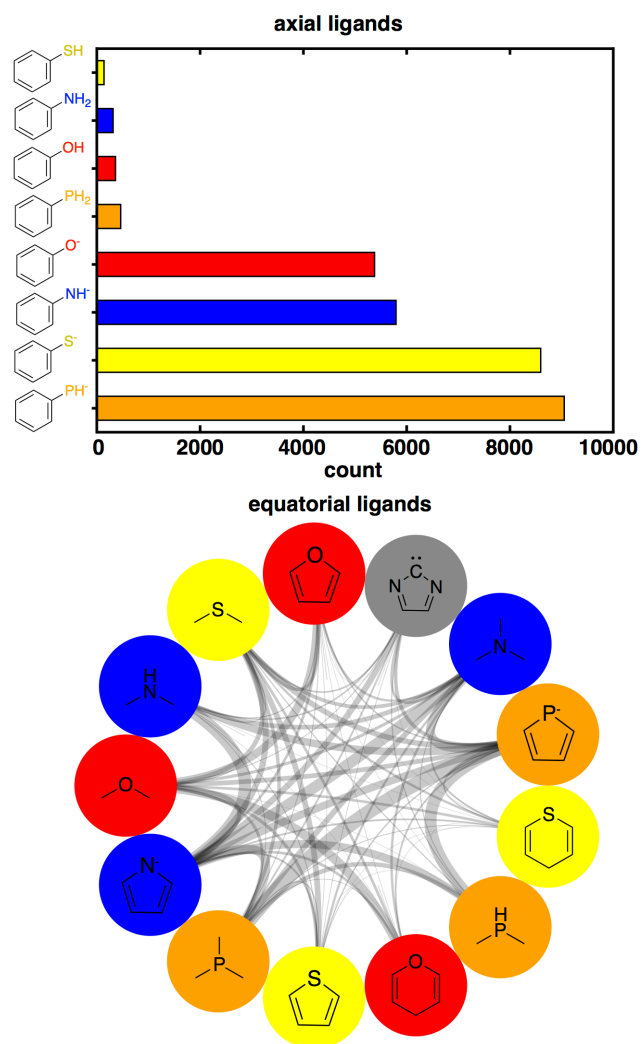


Figure 7. (top) axial ligands present within our energetic cutoff zone of 30,095 catalysts, colored by their metal coordinating atom with oxygen in red, nitrogen in blue, sulfur in yellow, and phosphorus in orange. (bottom) absolute frequencies of fragments that comprise equatorial ligands for catalysts in the cutoff zone, with chord thickness representing increased frequency of the pairs of fragments appearing within the cutoff zone. The circles containing the fragments are colored by the metal-coordinating atom identity, with carbon in gray, oxygen in red, nitrogen in blue, sulfur in yellow, and phosphorus in orange.

The source of this preference for anionic axial ligands in good catalyst designs could either be due to the lower field strength or how a charged ligand alters the charge on the metal center. To identify if the metal charge is altered, we computed the partial charges for resting state

catalysts from generations 0 to 3 and grouped them by axial ligand type (Figure 8 and Supporting Information Figure S32). Indeed, compounds with axial anionic ligands have metal centers with lower partial charge (i.e., are more neutral) due to increased charge transfer from the axial ligand. A series of one-tailed Welch's *t*-tests¹¹⁴ confirms that for all coordinating atom identities in our set (i.e., N, O, P, or S), compounds with negative axial ligands have less oxidized metal charge distributions than compounds with neutral axial ligands at a 5% significance level (Supporting Information Table S13). This lower positive partial charge on the metal should be expected to reduce electrostatic attraction to methanol, favoring its release. The axial ligand has a larger effect on release energetics than HAT, and we observe that $\Delta E(\text{HAT})$ distributions are unchanged as a function of axial anionic ligand (Supporting Information Figure S33). Analysis of the metal-oxo HOMO level, which has been used as a descriptor for $\Delta E(\text{HAT})$ reactivity¹⁰⁶, reveals it is more sensitive to equatorial ligand charge than axial ligand charge (Supporting Information Figure S34).

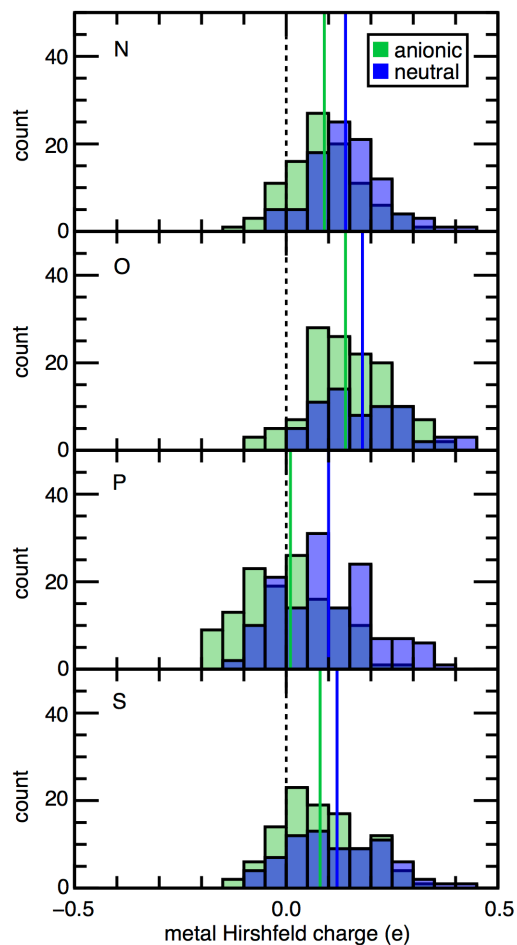


Figure 8. Metal Hirshfeld charge (in units of e) for catalysts from generations 0 to 3 with different axial ligands (N, O, P, S from top to bottom). Axial ligands are categorized into anionic (green) and neutral (blue) forms. The average Hirshfeld charge for anionic and neutral axial ligands are shown as green and blue lines respectively. A dotted black line indicates a metal Hirshfeld charge of 0.

We next explored whether we could obtain even further improved results in this already favorable set by again employing Hammett tuning. Adding functional groups to this subset of the catalyst space increases the number of compounds to over 412,000. Over this subspace of compounds, we are able to train models that have even smaller test set errors (<4 kcal/mol) than when we functionalized the full space, enabling us to predict the effects of functional group tuning more robustly (Supporting Information Table S14 and Figures S35–S37). Over three

additional generations of EGO, we find two additional Pareto optimal catalysts with functional groups that outperform any prior designs. One catalyst has an LS Fe(II) center in its ground spin state with strong field phosphole and trimethylphosphine fragments and trifluoromethyl functional groups (Supporting Information Figure S37 and Table S15). The other complex consists of an IS Mn(II) center in its ground spin state with a weak field equatorial macrocycle that is constructed from flexible oxygen fragments and amino-functionalized bridges (Supporting Information Figure S37 and Table S15). For this compound, the metal-oxo bond in the oxo intermediate has a strong tilt, which has been hypothesized to promote increased reactivity for Fe(IV)=O complexes⁴¹ (Supporting Information Figure S38).

For both our original functional group search and for this honed-in search, we observe more modest changes in the composition of the Pareto front than originally anticipated based on effects on porphyrin energetics. We hypothesized that the effects of functional groups were likely smaller in the case that the design space was enriched with non-aromatic compounds. To determine the relative percentage of aromatic compounds in our honed in design space, we estimated aromaticity in the equatorial macrocycles from their canonical SMILES string (Supporting Information Figure S39). Indeed, almost all (97%) compounds that are within the cutoff zone (i.e., the 30,095 compounds) have little-to-no aromaticity. This suggests that within our set of macrocycles non-aromatic compounds exhibit better reaction energetics than aromatic counterparts, despite the fact that porphyrinoid compounds¹¹⁵ that are frequently studied for C-H activation. Although some aromatic macrocycles fall within the cutoff zone, the best cases still have $\Delta E(\text{HAT})$ and $\Delta E(\text{release})$ energetics that are predicted by the ML models to be far (i.e., 8 to 10 kcal/mol) from the Pareto front in comparison to non-aromatic compounds (Supporting Information Figure S40). Thus, functional group tuning could be expected to alter the energetics

of aromatic macrocycles by a significant 5-15 kcal/mol margin, but most are too far from the Pareto front to surpass non-aromatic compounds even after functional group tuning. These observations further strengthen the case for ML-accelerated search of a wide macrocycle space rather than a focus on functional group tuning within a fixed macrocycle structure.

4.4 Catalytic Cycles of Pareto Optimal Catalysts.

To validate our best case catalyst designs, we completed the radical rebound catalytic cycle by computing additional reaction energies and barrier heights for the Pareto optimal catalysts that were identified by our honed in search. Because we optimized the catalysts for HAT and methanol release thermodynamics, we already know the reaction energetics of these steps are favorable. For HAT, a strong BEP relation means that favorable reaction energetics also correspond to favorable HAT kinetics. For methanol release, we model it as an unassisted dissociation and so we neglect any kinetic barrier. Thus, to complete the catalytic cycle, we next computed properties related to oxo formation and radical rebound.

Although strong Brønsted-Evans-Polanyi (BEP) relations between reaction energies and barrier heights have been invoked^{68, 71}, we observe these to only hold for HAT and not for oxo formation, consistent with prior work^{68, 73, 116} (Supporting Information Figures S41 and S42). Since thermodynamic scaling between oxo formation and HAT can be disrupted in molecular complexes²⁴, we had used EGO to optimize our catalysts for HAT and rebound with the expectation that oxo formation could still be favorable. Indeed, all eight Pareto optimal catalysts, two of which are in their ground spin states, have favorable oxo formation reaction energetics as well (Supporting Information Table S16). We obtained oxo formation barrier heights and approximate transition states (i.e., with NEB, see Computational Details) for the Pareto optimal

catalysts (Figure 9 and Supporting Information Table S16 and Figure S43). Indeed, we calculate a low barrier height (i.e., 5 kcal/mol) for oxo formation with our Pareto optimal IS Mn(II) catalyst that has a weak field oxygen-coordinating macrocycle (Figure 9 and Supporting Information Table S16 and Figure S43). This low barrier height is indeed correlated to the metal-oxo tilt we observed in the Mn(IV)=O intermediate (Supporting Information Figure S38). The oxo formation barrier for the Pareto optimal LS Fe(II) catalyst with strong field ligands is significantly higher (i.e., 25 kcal/mol) but still lower than what had been previously observed (> 30 kcal/mol) for Fe(II) model catalysts (Supporting Information Figure S43).

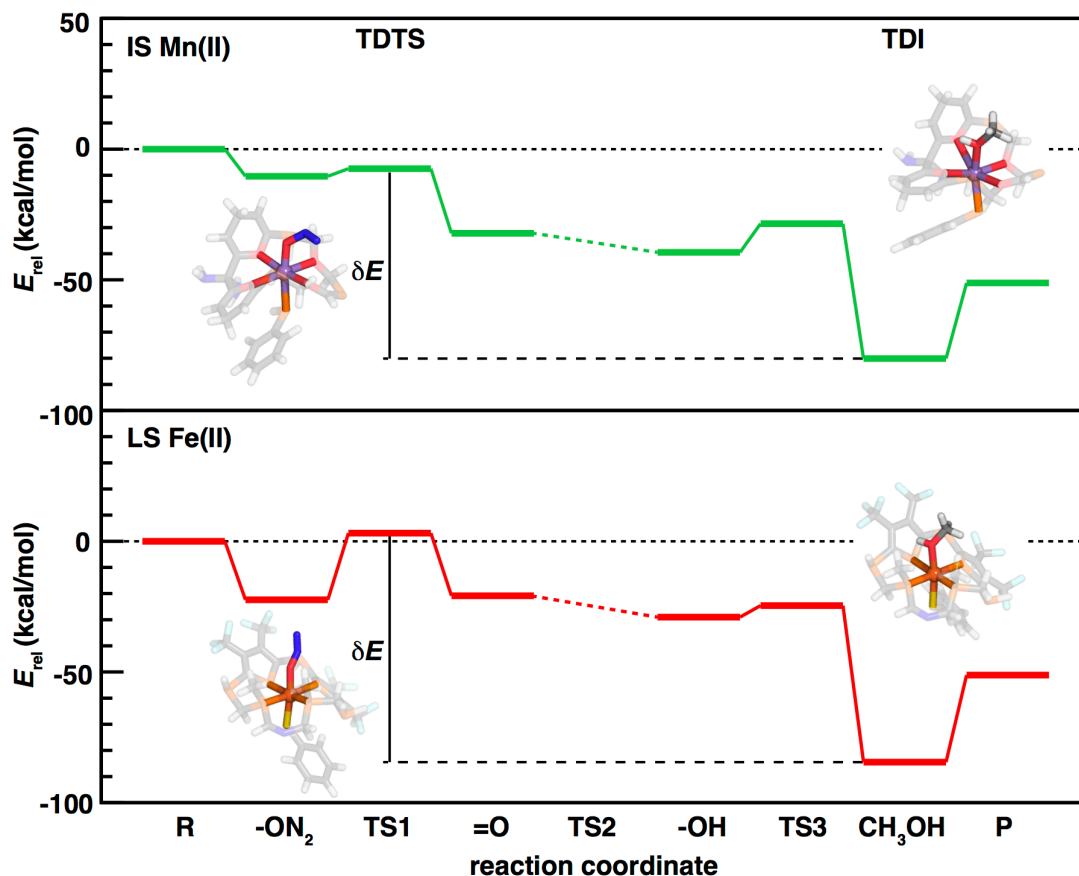


Figure 9. The full energy landscape of the two ground state Pareto optimal complexes with the Mn(II) lead complex (top), and Fe(II) lead complex (bottom) in green and red respectively. We draw the reaction coordinate from reactants (R) to products (P) through a metal-N₂O bound intermediate, the oxo formation transition state (TS1), the metal-oxo intermediate (=O), the hydrogen atom transfer transition state (TS2), the metal-hydroxyl intermediate (-OH), the

rebound transition state (TS3), and the metal-methanol bound intermediate. The turnover determining transition state (TDTS), and turnover determining intermediate (TDI) are shown inset, along with the energy span (δE) that governs efficient catalysis. HAT transition-states were found to be barrierless and are omitted, with neighboring steps connected by a dotted line.

Finally to complete the catalytic cycle, we also computed the kinetic barrier for the rebound step using potential energy scans in which the distance between the methyl radical and oxygen atom were constrained and all other degrees of freedom were relaxed (see Computational Details). This step is nearly barrierless in the Pareto optimal catalysts and thus cannot govern turnover on these catalysts (Supporting Information Figure S44). For the Pareto optimal IS Mn(II) catalyst, we find that the more stable oxo correspond to a higher (e.g. 10 kcal/mol) rebound barrier height, although this step still does not become a rate determining step (Figure 9 and Supporting Information Table S16 and Figure S44).

To identify the best catalyst of our two ground state Pareto-optimal catalysts, we use the energetic span model¹¹⁷ to approximate catalyst turnover frequencies. In all eight Pareto optimal catalysts, oxo formation is the turnover determining transition state (TDTS), and the methanol-bound intermediate is the turnover determining intermediate (TDI). Despite the moderate kinetic barriers for oxo formation from N₂O for all Pareto optimal catalysts, the improvements for methanol release thermodynamics relative to oxo formation kinetics make the expected catalytic performance of these identified complexes better than any HS Fe^{IV}=O catalysts that we have previously investigated⁷³ (Supporting Information Figure S43). We next calculate the energy spans of our two ground state Pareto optimal catalysts (Figure 9). Comparison of these systems to the model catalytic systems from prior work⁷³ indicates our Pareto optimal catalysts reduce the energy span by 15 kcal/mol, which corresponds to eleven orders of magnitude increase in

expected catalyst turnover frequency (Supporting Information Table S17 and Figure S45). Additionally, we find that the relative energetics and energy spans for methane oxidation on our Pareto optimal catalysts are comparable to the energy spans on multimetallic metal-organic framework (MOF) nodes^{45, 46} (Supporting Information Table S18). Nevertheless, this comparison is qualitative in nature due to the sensitivity of the TDTS and TDI energetics to functional choice for methane oxidation.¹¹⁸ The reduced oxo formation activation barrier heights and improved thermodynamics for methanol release energetics that correspond to smaller energy spans on our macrocyclic catalysts compared to previous model systems demonstrate that our ML-accelerated EGO strategy can uncover new and more efficient catalysts. Further catalyst designs will focus on designing pentadentate scaffolds that can simultaneously incorporate effects of increased out-of-plane distortion that can further reduce oxo formation barriers, while also quantifying the effect of oxidant (i.e., N₂O vs. O₂) choice on barrier heights.

5. Conclusions.

Catalyst design requires consideration of tradeoffs between different steps on the catalyst energy landscape that are difficult to optimize by trial and error alone. As LFERs and BEP relations seldom hold strongly in single-site catalysis, these trade-offs are not readily captured by descriptor-based screening, suggesting the possibility to overcome present limitations in the design of active methane-to-methanol catalysts. To leverage these possibilities and overcome the limitations or prior approaches, we used EGO to optimize two reaction energies for two steps in the radical rebound mechanism for direct methane-to-methanol conversion. We constructed a nearly 2M compound space of catalysts comprised of oft-studied Mn and Fe centers combined with equatorial ligands constructed from fragments inspired by synthesized macrocycles. With this strategy, we recovered existing chemistry (e.g., porphyrins, corroles, and phthalocyanines)

while introducing novel, underexplored compounds. By using EGO in combination with ANN models we identified novel low spin Fe(II) compounds were often paired with strong field (e.g. P or S-coordinating) axial ligands that differed from more commonly studied high-spin Fe(II) catalysts with weak field ligands.

To mimic Hammett tuning commonly employed in catalyst screening, we added functional groups to fragments and bridges of our macrocycles, thereby expanding our candidate space to nearly 16M compounds. Because the most favorable macrocycles lack aromaticity, the improvement of reaction energetics achieved by changing the macrocycle or axial ligand exceeded what could be achieved through functionalization. Nevertheless, the majority of the final Pareto optimal set from this screen consisted of catalysts only identified after a full six generations of EGO. To refine our search, we downselected to a subset of favorable catalysts prior to functionalization. Over this set, we both improved model performance and observed that the best tradeoff between HAT and methanol release occurred when catalysts had negatively charged axial ligands that correlated to facile methanol release.

Finally, we computed the kinetic barriers alongside reaction thermodynamics for the radical rebound mechanism in methane-to-methanol conversion of the Pareto optimal catalysts. As EGO was used to optimize catalysts for HAT and methanol release, we focused on determining if this led to any deleterious effect on oxo formation or radical rebound. Analysis of these steps revealed that all Pareto optimal catalysts form metal-oxos favorably and have modest N_2O barrier heights relative to previously studied catalysts. At the same time, the radical rebound step is never rate determining. Thus, our catalyst screening strategy captured the key steps to optimize for this reaction mechanism. Energetic span analysis on the two lead compounds in their ground state spin, an IS Mn(II) catalyst and a LS Fe(II) catalyst, revealed both had

favorable energetics that would lead to reasonable turnover frequencies. Our 2D-EI approach on *in silico* synthesized macrocycles represents a promising strategy for rapidly optimizing decoupled reaction steps and is expected to be general to other reaction systems in homogeneous catalysis.

6. Methods

Gas-phase geometry optimizations and single-point energy calculations were performed using density functional theory (DFT) with a development version of TeraChem v1.9.¹¹⁹ The B3LYP¹²⁰⁻¹²² global hybrid functional with the empirical D3 dispersion correction¹²³ using Becke–Johnson damping¹²⁴ was employed for all calculations. The LACVP* composite basis set was employed throughout this work, which consists of a LANL2DZ effective core potential¹²⁵,¹²⁶ for Mn, Fe, Br, and I, and the 6-31G* basis¹²⁷ for all other atoms. As in prior work, we focus on relative energetics over a large data set, and we neglect solvent corrections and zero-point vibrational energy or entropic corrections to avoid a significant increase in computational cost.²⁴

Singlet calculations were carried out in a spin-restricted formalism following prior work²⁴, whereas all other spin states were performed as unrestricted calculations. The convention of majority-spin addition of radicals is employed throughout. Level shifting¹²⁸ of 0.25 Ha was applied to both majority and minority spin virtual orbitals to aid self-consistent field (SCF) convergence to an unrestricted solution. Geometry optimizations were carried out with the translation rotation internal coordinate (TRIC) optimizer¹²⁹ using the L-BFGS algorithm. Default tolerances in the convergence criteria were employed for the maximum energy gradient of 4.5×10^{-4} hartree/bohr and energy difference between steps of 10^{-6} hartree. The initial geometries for metal–oxo species were constructed using molSimplify,¹³⁰ which uses OpenBabel^{131, 132} as a backend to interpret SMILES strings. Tetradentate macrocycle SMILES strings were constructed

using custom algorithms available in molSimplify and validated using RDKit version 2020.03.2.¹³³ We oriented any methyl groups on metal-coordinating atoms *syn* relative to the metal-oxo to follow the most common isomer in experimentally characterized metal-oxo compounds.¹³⁴⁻¹³⁶

Job submission was automated by molSimplify with a 24 h wall time per run with up to five resubmissions. Geometry optimizations were carried out with geometry checks¹³⁷ prior to each resubmission and structures that failed any check were eliminated (Supporting Information Table S19). Open-shell structures were also removed from the data set following established protocols^{80, 88, 137} if the expectation value of the S^2 operator deviated from its expected value of $S(S + 1)$ by $>1 \mu_B^2$ or the combined Mulliken spin density on the metal and oxygen differed from the spin multiplicity by $>1 \mu_B$. We employed a machine learning strategy to predict calculation failure from the electronic¹³⁷ using a multitask neural network classifier¹³⁸ applied up to the first forty steps of the geometry optimization (Supporting Information Tables S19–S21 and Figure S46).

In addition to metal–oxo intermediates, other radical rebound intermediates are generated in the following sequence. All metal–hydroxo geometries were generated by adding an H atom to the optimized metal–oxo structure, and all methanol-bound intermediates were generated by adding a methyl group to the optimized metal–hydroxo structures using a custom script in molSimplify, as in prior work²⁴ (Supporting Information Figures S47 and S48). Resting state catalyst structures are obtained as single-point energies after removal of the methanol molecule from methanol-bound intermediates. The workflow starts by optimizing the metal–oxo geometry, and if this or a subsequent intermediate does not succeed, downstream intermediate optimizations are not attempted.

Approximate transition states (TSs) for N₂O activation were modeled with nudged elastic band (NEB) method with climbing image^{139, 140} as implemented in the TeraChem^{119, 141} interface to DL-FIND¹⁴². Approximate TSs for the radical rebound step were obtained via a series of constrained optimizations in which the metal-oxo oxygen and methyl radical carbon distance was scanned from 2.6 Å to 1.4 Å in 0.1 Å increments while letting all other atoms relax.

ASSOCIATED CONTENT

Supporting Information. The following files are available free of charge.

Spin and oxidation state definitions; reference energetics for all small molecules used for reaction energies; criteria used for geometry and electronic structure checks; dynamic classification latent space entropy cutoffs and comparisons; details of workflows for reactive intermediate functionalization; examples of macrocycle construction; macrocycles eliminated due to repeats; counts of ring sizes in macrocycles; statistics on macrocycles with different coordinating atoms; duplicate complexes in RAC space; comparisons of hypothetical compounds to synthesized compounds; visual and mathematical explanation of 2D-expected improvement; relationship between HAT and methanol release energetics; failure rate statistics and *k*-medoids sampling for generation 0; hyperparameters for all ANN models; comparison between ANN and GP model performance; timing for one full generation of EGO; demonstration of EI by generation; train-validation-test set splits; ANN performance by generation; evolution of Pareto optimal catalysts over time; rules for functionalizing macrocycles on fragments and bridges; analyses on functionalization effects on metal charges and HOMO levels; SHAP analysis on ANNs with functionalized macrocycles; changes in chemical space diversity while subsampling ligand space; statistical analyses of metal Hirshfeld charges; effects of net charge on frontier orbital energies; analyses of spin splitting energies for lead complexes; identification of aromaticity via SMILES; verification of BEP principle for oxo formation and HAT; full energy landscapes for Pareto optimal catalysts; transition state structures for N₂O activation; kinetic barriers for radical rebound; comparison to existing catalysts for light alkane activation. (PDF)

Structures for all reactive intermediates for all generations; structures for approximate transition states; raw electronic energies and reaction energies for all catalysts in all generations; and train-validation-test data splits at each generation. (ZIP)

AUTHOR INFORMATION

Notes

The authors declare no competing financial interests.

ACKNOWLEDGMENT

This work is supported as part of the Inorganometallic Catalysis Design Center, an Energy Frontier Research Center funded by the U.S. Department of Energy, Office of Science, Basic Energy Sciences under Award DE-SC0012702 (to A.N. and H.J.K.). The authors also acknowledge support by DARPA (grant number D18AP00039) for the active learning efforts, and some of the algorithmic developments were supported by the Office of Naval Research under grant number N00014-20-1-2150 (to C.D. and H.J.K.). C.G. was supported by the National Science Foundation grant number CBET-1704266. This work was also partially supported by a National Science Foundation Graduate Research Fellowship under Grant #1122374 (to A.N.). H.J.K. holds a Career Award at the Scientific Interface from the Burroughs Wellcome Fund, an AAAS Marion Milligan Mason Award, and an Alfred P. Sloan Fellowship in Chemistry, which supported this work. The authors thank Akash Bajaj, Adam H. Steeves, Shuwen Yue, and Vyshnavi Vennelakanti for providing a critical reading of the manuscript.

REFERENCES

1. Olah, G. A., Beyond Oil and Gas: the Methanol Economy. *Angew. Chem., Int. Ed.* **2005**, *44* (18), 2636-2639.
2. Lunsford, J. H., Catalytic Conversion of Methane to More Useful Chemicals and Fuels: a Challenge for the 21st Century. *Catal. Today* **2000**, *63* (2), 165-174.
3. Ravi, M.; Ranocchiari, M.; van Bokhoven, J. A., The Direct Catalytic Oxidation of Methane to Methanol-A Critical Assessment. *Angew. Chem., Int. Ed.* **2017**, *56* (52), 16464-16483.
4. Tomkins, P.; Ranocchiari, M.; van Bokhoven, J. A., Direct Conversion of Methane to Methanol under Mild Conditions over Cu-Zeolites and beyond. *Acc. Chem. Res.* **2017**, *50* (2), 418-425.
5. Latimer, A. A.; Kakekhani, A.; Kulkarni, A. R.; Nørskov, J. K., Direct Methane to Methanol: The Selectivity–Conversion Limit and Design Strategies. *ACS Catal.* **2018**, *8* (8), 6894-6907.
6. Price, J. C.; Barr, E. W.; Glass, T. E.; Krebs, C.; Bollinger, J. M., Evidence for Hydrogen Abstraction from C1 of Taurine by the High-Spin Fe(IV) Intermediate Detected

During Oxygen Activation by Taurine: α -Ketoglutarate Dioxygenase (TauD). *J. Am. Chem. Soc.* **2003**, *125* (43), 13008-13009.

7. Price, J. C.; Barr, E. W.; Tirupati, B.; Bollinger, J. M.; Krebs, C., The First Direct Characterization of a High-Valent Iron Intermediate in the Reaction of an α -Ketoglutarate-Dependent Dioxygenase: a High-Spin Fe(IV) Complex in Taurine/ α -Ketoglutarate Dioxygenase (TauD) from Escherichia Coli. *Biochemistry* **2003**, *42* (24), 7497-7508.

8. Eichhorn, E.; van der Ploeg, J. R.; Kertesz, M. A.; Leisinger, T., Characterization of α -Ketoglutarate-Dependent Taurine Dioxygenase from Escherichia Coli. *J. Biol. Chem.* **1997**, *272* (37), 23031-23036.

9. Zilly, F. E.; Acevedo, J. P.; Augustyniak, W.; Deege, A.; Häusig, U. W.; Reetz, M. T., Tuning a P450 Enzyme for Methane Oxidation. *Angew. Chem., Int. Ed.* **2011**, *50* (12), 2720-2724.

10. Chen, M. M.; Coelho, P. S.; Arnold, F. H., Utilizing Terminal Oxidants to Achieve P450-Catalyzed Oxidation of Methane. *Adv. Synth. Catal.* **2012**, *354* (6), 964-968.

11. Oloo, W., N.; Que, L., Jr., Bioinspired Nonheme Iron Catalysts for C-H and C-C Bond Oxidation: Insights into the Nature of the Metal-Based Oxidants. *Acc. Chem. Res.* **2015**, *48* (9), 2612-2621.

12. Que, L., Jr.; Tolman, W. B., Biologically Inspired Oxidation Catalysis. *Nature* **2008**, *455* (7211), 333-340.

13. Biswas, A. N.; Puri, M.; Meier, K. K.; Oloo, W. N.; Rohde, G. T.; Bominaar, E. L.; Munck, E.; Que, L., Jr., Modeling TauD-J: a High-Spin Nonheme Oxoiron(IV) Complex with High Reactivity Toward C-H Bonds. *J. Am. Chem. Soc.* **2015**, *137* (7), 2428-2431.

14. Engelmann, X.; Monte-Perez, I.; Ray, K., Oxidation Reactions with Bioinspired Mononuclear Non-Heme Metal-Oxo Complexes. *Angew. Chem., Int. Ed.* **2016**, *55* (27), 7632-7649.

15. Periana, R. A.; Taube, D. J.; Gamble, S.; Taube, H.; Satoh, T.; Fujii, H., Platinum Catalysts for the High-Yield Oxidation of Methane to a Methanol Derivative. *Science* **1998**, *280* (5363), 560-564.

16. Muehlhofer, M.; Strassner, T.; Herrmann, W. A., New Catalyst Systems for the Catalytic Conversion of Methane into Methanol. *Angew. Chem., Int. Ed.* **2002**, *41* (10), 1745-1747.

17. Shilov, A. E.; Shul'pin, G. B., Activation of C-H Bonds by Metal Complexes. *Chem. Rev.* **1997**, *97* (8), 2879-2932.

18. Jones, C.; Taube, D.; Ziatdinov, V. R.; Periana, R. A.; Nielsen, R. J.; Oxgaard, J.; Goddard, W. A., Selective Oxidation of Methane to Methanol Catalyzed, with C-H Activation, by Homogeneous, Cationic Gold. *Angew. Chem., Int. Ed.* **2004**, *116* (35), 4726-4729.

19. Palkovits, R.; Antonietti, M.; Kuhn, P.; Thomas, A.; Schüth, F., Solid Catalysts for the Selective Low-Temperature Oxidation of Methane to Methanol. *Angew. Chem., Int. Ed.* **2009**, *48* (37), 6909-6912.

20. Dinh, K. T.; Sullivan, M. M.; Serna, P.; Meyer, R. J.; Dincă, M.; Román-Leshkov, Y., Viewpoint on the Partial Oxidation of Methane to Methanol Using Cu- and Fe-Exchanged Zeolites. *ACS Catal.* **2018**, *8* (9), 8306-8313.

21. Szécsényi, Á.; Li, G.; Gascon, J.; Pidko, E. A., Mechanistic Complexity of Methane Oxidation with H₂O₂ by Single-Site Fe/ZSM-5 Catalyst. *ACS Catal.* **2018**, *8* (9), 7961-7972.

22. Vogiatzis, K. D.; Haldoupis, E.; Xiao, D. J.; Long, J. R.; Siepmann, J. I.; Gagliardi, L., Accelerated Computational Analysis of Metal-Organic Frameworks for Oxidation Catalysis. *J. Phys. Chem. C* **2016**, *120* (33), 18707-18712.

23. Borovik, A. S., Role of Metal-Oxo Complexes in the Cleavage of C-H Bonds. *Chem. Soc. Rev.* **2011**, *40* (4), 1870-4.
24. Nandy, A.; Kulik, H. J., Why Conventional Design Rules for C-H Activation Fail for Open-Shell Transition-Metal Catalysts. *ACS Catal.* **2020**, *10* (24), 15033-15047.
25. Nam, W., Synthetic Mononuclear Nonheme Iron-Oxygen Intermediates. *Acc. Chem. Res.* **2015**, *48* (8), 2415-2423.
26. Nam, W.; Lee, Y.-M.; Fukuzumi, S., Tuning Reactivity and Mechanism in Oxidation Reactions by Mononuclear Nonheme Iron(IV)-Oxo Complexes. *Acc. Chem. Res.* **2014**, *47* (4), 1146-1154.
27. Monte Pérez, I.; Engelmann, X.; Lee, Y.-M.; Yoo, M.; Kumaran, E.; Farquhar, E. R.; Bill, E.; England, J.; Nam, W.; Swart, M.; Ray, K., A Highly Reactive Oxoiron(IV) Complex Supported by a Bioinspired N₃O Macrocyclic Ligand. *Angew. Chem., Int. Ed.* **2017**, *56* (46), 14384-14388.
28. Yadav, V.; Rodriguez, R. J.; Siegler, M. A.; Goldberg, D. P., Determining the Inherent Selectivity for Carbon Radical Hydroxylation versus Halogenation with Fe^{III}(OH)(X) Complexes: Relevance to the Rebound Step in Non-heme Iron Halogenases. *J. Am. Chem. Soc.* **2020**, *142* (16), 7259-7264.
29. Rosen, A. S.; Notestein, J. M.; Snurr, R. Q., Structure–Activity Relationships That Identify Metal–Organic Framework Catalysts for Methane Activation. *ACS Catal.* **2019**, *9* (4), 3576-3587.
30. Osadchii, D. Y.; Olivos-Suarez, A. I.; Szécsényi, Á.; Li, G.; Nasalevich, M. A.; Dugulan, I. A.; Crespo, P. S.; Hensen, E. J.; Veber, S. L.; Fedin, M. V., Isolated Fe Sites in Metal Organic Frameworks Catalyze the Direct Conversion of Methane to Methanol. *ACS Catal.* **2018**, *8* (6), 5542-5548.
31. Snyder, B. E. R.; Böttger, L. H.; Bols, M. L.; Yan, J. J.; Rhoda, H. M.; Jacobs, A. B.; Hu, M. Y.; Zhao, J.; Alp, E. E.; Hedman, B.; Hodgson, K. O.; Schoonheydt, R. A.; Sels, B. F.; Solomon, E. I., Structural Characterization of a Non-Heme Iron Active Site in Zeolites that Hydroxylates Methane. *Proc. Natl. Acad. Sci. U.S.A.* **2018**, *115* (18), 4565-4570.
32. Snyder, B. E. R.; Vanelderen, P.; Bols, M. L.; Hallaert, S. D.; Böttger, L. H.; Ungur, L.; Pierloot, K.; Schoonheydt, R. A.; Sels, B. F.; Solomon, E. I., The Active Site of Low-Temperature Methane Hydroxylation in Iron-Containing Zeolites. *Nature* **2016**, *536* (7616), 317-321.
33. Xiao, D. J.; Bloch, E. D.; Mason, J. A.; Queen, W. L.; Hudson, M. R.; Planas, N.; Borycz, J.; Dzubak, A. L.; Verma, P.; Lee, K.; Bonino, F.; Crocella, V.; Yano, J.; Bordiga, S.; Truhlar, D. G.; Gagliardi, L.; Brown, C. M.; Long, J. R., Oxidation of Ethane to Ethanol by N₂O in a Metal-Organic Framework with Coordinatively Unsaturated Iron(II) Sites. *Nat. Chem.* **2014**, *6* (7), 590-595.
34. Simons, M. C.; Prinslow, S. D.; Babucci, M.; Hoffman, A. S.; Hong, J.; Vitillo, J. G.; Bare, S. R.; Gates, B. C.; Lu, C. C.; Gagliardi, L.; Bhan, A., Beyond Radical Rebound: Methane Oxidation to Methanol Catalyzed by Iron Species in Metal–Organic Framework Nodes. *J. Am. Chem. Soc.* **2021**, *143* (31), 12165-12174.
35. Simons, M. C.; Vitillo, J. G.; Babucci, M.; Hoffman, A. S.; Boubnov, A.; Beauvais, M. L.; Chen, Z.; Cramer, C. J.; Chapman, K. W.; Bare, S. R.; Gates, B. C.; Lu, C. C.; Gagliardi, L.; Bhan, A., Structure, Dynamics, and Reactivity for Light Alkane Oxidation of Fe(II) Sites Situated in the Nodes of a Metal–Organic Framework. *J. Am. Chem. Soc.* **2019**, *141* (45), 18142-18151.

36. Rohde, J. U.; In, J. H.; Lim, M. H.; Brennessel, W. W.; Bukowski, M. R.; Stubna, A.; Munck, E.; Nam, W.; Que, L., Jr., Crystallographic and Spectroscopic Characterization of a Nonheme Fe(IV)-O Complex. *Science* **2003**, *299* (5609), 1037-1039.
37. Pestovsky, O.; Stoian, S.; Bominaar, E. L.; Shan, X.; Munck, E.; Que, L., Jr.; Bakac, A., Aqueous Fe^{IV}=O: Spectroscopic Identification and Oxo-Group Exchange. *Angew. Chem., Int. Ed.* **2005**, *44* (42), 6871-6874.
38. Grapperhaus, C. A.; Mienert, B.; Bill, E.; Weyhermüller, T.; Wieghardt, K., Mononuclear (Nitrido)Iron(V) and (Oxo)Iron(IV) Complexes via Photolysis of [(cyclam-acetato)Fe^{III}(N₃)]⁺ and Ozonolysis of [(cyclam-acetato)Fe^{III}(O₃SCF₃)]⁺ in Water/Acetone Mixtures. *Inorg. Chem.* **2000**, *39* (23), 5306-5317.
39. Ehudin, M. A.; Gee, L. B.; Sabuncu, S.; Braun, A.; Moënne-Loccoz, P.; Hedman, B.; Hodgson, K. O.; Solomon, E. I.; Karlin, K. D., Tuning the Geometric and Electronic Structure of Synthetic High-Valent Heme Iron(IV)-Oxo Models in the Presence of a Lewis Acid and Various Axial Ligands. *J. Am. Chem. Soc.* **2019**, *141* (14), 5942-5960.
40. Klinker, E. J.; Kaizer, J.; Brennessel, W. W.; Woodrum, N. L.; Cramer, C. J.; Que, L., Jr., Structures of Nonheme Oxoiron(IV) Complexes from X-ray crystallography, NMR Spectroscopy, and DFT Calculations. *Angew. Chem., Int. Ed.* **2005**, *44* (24), 3690-3694.
41. Rasheed, W.; Draksharapu, A.; Banerjee, S.; Young, V. G.; Fan, R.; Guo, Y.; Ozerov, M.; Nehrkorn, J.; Krzystek, J.; Telser, J.; Que, L., Crystallographic Evidence for a Sterically Induced Ferryl Tilt in a Non-Heme Oxoiron(IV) Complex that Makes it a Better Oxidant. *Angew. Chem., Int. Ed.* **2018**, *130* (30), 9531-9535.
42. Raugei, S.; DuBois, D. L.; Rousseau, R.; Chen, S.; Ho, M.-H.; Bullock, R. M.; Dupuis, M., Toward Molecular Catalysts by Computer. *Acc. Chem. Res.* **2015**, *48* (2), 248-255.
43. Thiel, W., Computational Catalysis—Past, Present, and Future. *Angew. Chem., Int. Ed.* **2014**, *53* (33), 8605-8613.
44. Rice, D. B.; Massie, A. A.; Jackson, T. A., Experimental and Multireference Ab Initio Investigations of Hydrogen-Atom-Transfer Reactivity of a Mononuclear Mn^{IV}-Oxo Complex. *Inorg. Chem.* **2019**, *58* (20), 13902-13916.
45. Vitillo, J. G.; Bhan, A.; Cramer, C. J.; Lu, C. C.; Gagliardi, L., Quantum Chemical Characterization of Structural Single Fe(II) Sites in MIL-Type Metal–Organic Frameworks for the Oxidation of Methane to Methanol and Ethane to Ethanol. *ACS Catal.* **2019**, *9* (4), 2870-2879.
46. Barona, M.; Ahn, S.; Morris, W.; Hoover, W.; Notestein, J. M.; Farha, O. K.; Snurr, R. Q., Computational Predictions and Experimental Validation of Alkane Oxidative Dehydrogenation by Fe₂M MOF Nodes. *ACS Catal.* **2019**, *10* (2), 1460-1469.
47. Verma, P.; Vogiatzis, K. D.; Planas, N.; Borycz, J.; Xiao, D. J.; Long, J. R.; Gagliardi, L.; Truhlar, D. G., Mechanism of Oxidation of Ethane to Ethanol at Iron(IV)-Oxo Sites in Magnesium-Diluted Fe₂(dobdc). *J. Am. Chem. Soc.* **2015**, *137*, 5770-5781.
48. Song, W. J.; Seo, M. S.; DeBeer George, S.; Ohta, T.; Song, R.; Kang, M.-J.; Tosha, T.; Kitagawa, T.; Solomon, E. I.; Nam, W., Synthesis, Characterization, and Reactivities of Manganese(V)-Oxo Porphyrin Complexes. *J. Am. Chem. Soc.* **2007**, *129* (5), 1268-1277.
49. Massie, A. A.; Denler, M. C.; Cardoso, L. T.; Walker, A. N.; Hossain, M. K.; Day, V. W.; Nordlander, E.; Jackson, T. A., Equatorial Ligand Perturbations Influence the Reactivity of Manganese(IV)-Oxo Complexes. *Angew. Chem., Int. Ed.* **2017**, *56* (15), 4178-4182.

50. Klein, J. E.; Knizia, G., cPCET versus HAT: A Direct Theoretical Method for Distinguishing X–H Bond-Activation Mechanisms. *Angew. Chem., Int. Ed.* **2018**, *130* (37), 12089-12093.
51. Shaik, S.; Chen, H.; Janardanan, D., Exchange-Enhanced Reactivity in Bond Activation by Metal-Oxo Enzymes and Synthetic Reagents. *Nat. Chem.* **2011**, *3* (1), 19-27.
52. Janardanan, D.; Wang, Y.; Schyman, P.; Que, L., Jr.; Shaik, S., The Fundamental Role of Exchange-Enhanced Reactivity in C-H Activation by S=2 Oxo Iron(IV) Complexes. *Angew. Chem., Int. Ed.* **2010**, *49* (19), 3342-3345.
53. Venturinelli Jannuzzi, S. A.; Phung, Q. M.; Domingo, A.; Formiga, A. L.; Pierloot, K., Spin State Energetics and Oxo Character of Mn-Oxo Porphyrins by Multiconfigurational ab Initio Calculations: Implications on Reactivity. *Inorg. Chem.* **2016**, *55* (11), 5168-79.
54. Gupta, R.; Lacy, D. C.; Bominaar, E. L.; Borovik, A. S.; Hendrich, M. P., Electron Paramagnetic Resonance and Mossbauer Spectroscopy and Density Functional Theory Analysis of a High-Spin Fe(IV)-Oxo Complex. *J. Am. Chem. Soc.* **2012**, *134* (23), 9775-9784.
55. Rosen, A. S.; Notestein, J. M.; Snurr, R. Q., High-Valent Metal–Oxo Species at the Nodes of Metal–Triazolate Frameworks: The Effects of Ligand Exchange and Two-State Reactivity for C–H Bond Activation. *Angew. Chem., Int. Ed.* **2020**.
56. Geng, C.; Ye, S.; Neese, F., Analysis of Reaction Channels for Alkane Hydroxylation by Nonheme Iron(IV)-Oxo Complexes. *Angew. Chem., Int. Ed.* **2010**, *49* (33), 5717-5720.
57. Geng, C.; Ye, S.; Neese, F., Does a Higher Metal Oxidation State Necessarily Imply Higher Reactivity toward H-atom Transfer? A Computational Study of C–H Bond Oxidation by High-Valent Iron-Oxo and -Nitrido Complexes. *Dalton Trans.* **2014**, *43* (16), 6079.
58. Ye, S.; Geng, C. Y.; Shaik, S.; Neese, F., Electronic Structure Analysis of Multistate Reactivity in Transition Metal Catalyzed Reactions: the Case of C-H Bond Activation by Non-heme Iron(IV)-oxo Cores. *Phys. Chem. Chem. Phys.* **2013**, *15* (21), 8017-8030.
59. Kupper, C.; Mondal, B.; Serrano-Plana, J.; Klawitter, I.; Neese, F.; Costas, M.; Ye, S.; Meyer, F., Nonclassical Single-State Reactivity of an Oxo-Iron(IV) Complex Confined to Triplet Pathways. *J. Am. Chem. Soc.* **2017**, *139* (26), 8939-8949.
60. Shaik, S.; Hirao, H.; Kumar, D., Reactivity of High-Valent Iron-Oxo Species in Enzymes and Synthetic Reagents: a Tale of Many States. *Acc. Chem. Res.* **2007**, *40* (7), 532-542.
61. Busch, M.; Fabrizio, A.; Lubner, S.; Hutter, J.; Corminboeuf, C., Exploring the Limitation of Molecular Water Oxidation Catalysts. *J. Phys. Chem. C* **2018**, *122* (23), 12404-12412.
62. Wodrich, M. D.; Sawatlon, B.; Busch, M.; Corminboeuf, C., The Genesis of Molecular Volcano Plots. *Acc. Chem. Res.* **2021**, *54* (5), 1107-1117.
63. Abild-Pedersen, F.; Greeley, J.; Studt, F.; Rossmeisl, J.; Munter, T. R.; Moses, P. G.; Skulason, E.; Bligaard, T.; Nørskov, J. K., Scaling Properties of Adsorption Energies for Hydrogen Containing Molecules on Transition-Metal Surfaces. *Phys. Rev. Lett.* **2007**, *99* (1), 016105.
64. Nørskov, J. K.; Bligaard, T.; Rossmeisl, J.; Christensen, C. H., Towards the Computational Design of Solid Catalysts. *Nat. Chem.* **2009**, *1* (1), 37-46.
65. Busch, M.; Wodrich, M. D.; Corminboeuf, C., Linear Scaling Relationships and Volcano Plots in Homogeneous Catalysis – Revisiting the Suzuki Reaction. *Chem. Sci.* **2015**, *6* (12), 6754-6761.

66. Meyer, B.; Sawatlon, B.; Heinen, S.; von Lilienfeld, O. A.; Corminboeuf, C., Machine Learning Meets Volcano Plots: Computational Discovery of Cross-Coupling Catalysts. *Chem. Sci.* **2018**, *9* (35), 7069-7077.
67. Wodrich, M. D.; Sawatlon, B.; Busch, M.; Corminboeuf, C., On the Generality of Molecular Volcano Plots. *ChemCatChem* **2018**, *10* (7), 1586-1591.
68. Latimer, A. A.; Kulkarni, A. R.; Aljama, H.; Montoya, J. H.; Yoo, J. S.; Tsai, C.; Abild-Pedersen, F.; Studt, F.; Nørskov, J. K., Understanding Trends in C-H Bond Activation in Heterogeneous Catalysis. *Nat. Mater.* **2017**, *16* (2), 225-229.
69. Vogiatzis, K. D.; Polynski, M. V.; Kirkland, J. K.; Townsend, J.; Hashemi, A.; Liu, C.; Pidko, E. A., Computational Approach to Molecular Catalysis by 3d Transition Metals: Challenges and Opportunities. *Chem. Rev.* **2018**, *119* (4), 2453-2523.
70. Wodrich, M. D.; Busch, M.; Corminboeuf, C., Accessing and Predicting the Kinetic Profiles of Homogeneous Catalysts from Volcano Plots. *Chem. Sci.* **2016**, *7*, 5723-5735.
71. Wodrich, M. D.; Sawatlon, B.; Solel, E.; Kozuch, S.; Corminboeuf, C., Activity-Based Screening of Homogeneous Catalysts through the Rapid Assessment of Theoretically Derived Turnover Frequencies. *ACS Catal.* **2019**, *9* (6), 5716-5725.
72. Chantarojsiri, T.; Reath, A. H.; Yang, J. Y., Cationic Charges Leading to an Inverse Free-Energy Relationship for N-N Bond Formation by Mn^{VI} Nitrides. *Angew. Chem., Int. Ed.* **2018**, *57* (43), 14037-14042.
73. Gani, T. Z. H.; Kulik, H. J., Understanding and Breaking Scaling Relations in Single-Site Catalysis: Methane to Methanol Conversion by Fe^{IV}=O. *ACS Catal.* **2018**, *8*, 975-986.
74. Darby, M. T.; Stamatakis, M.; Michaelides, A.; Sykes, E. C. H., Lonely Atoms with Special Gifts: Breaking Linear Scaling Relationships in Heterogeneous Catalysis with Single-Atom Alloys. *J. Phys. Chem. Lett.* **2018**, *9* (18), 5636-5646.
75. Zandkarimi, B.; Alexandrova, A. N., Dynamics of Subnanometer Pt Clusters Can Break the Scaling Relationships in Catalysis. *J. Phys. Chem. Lett.* **2019**, *10* (3), 460-467.
76. Pérez-Ramírez, J.; López, N., Strategies to Break Linear Scaling Relationships. *Nat. Catal.* **2019**, *2* (11), 971-976.
77. Chantarojsiri, T.; Sun, Y.; Long, J. R.; Chang, C. J., Water-Soluble Iron(IV)-Oxo Complexes Supported by Pentapyridine Ligands: Axial Ligand Effects on Hydrogen Atom and Oxygen Atom Transfer Reactivity. *Inorg. Chem.* **2015**, *54* (12), 5879-87.
78. Cavallo, L.; Jacobsen, H., Electronic Effects in (salen)Mn-Based Epoxidation Catalysts. *The Journal of Organic Chemistry* **2003**, *68* (16), 6202-6207.
79. Nandy, A.; Duan, C.; Taylor, M. G.; Liu, F.; Steeves, A. H.; Kulik, H. J., Computational Discovery of Transition-metal Complexes: From High-throughput Screening to Machine Learning. *Chem. Rev.* **2021**, *121* (16), 9927-10000.
80. Nandy, A.; Zhu, J.; Janet, J. P.; Duan, C.; Getman, R. B.; Kulik, H. J., Machine Learning Accelerates the Discovery of Design Rules and Exceptions in Stable Metal-Oxo Intermediate Formation. *ACS Catal.* **2019**, *9*, 8243-8255.
81. Friederich, P.; dos Passos Gomes, G.; De Bin, R.; Aspuru-Guzik, A.; Balcells, D., Machine Learning Dihydrogen Activation in the Chemical Space Surrounding Vaska's Complex. *Chem. Sci.* **2020**, *11* (18), 4584-4601.
82. dos Passos Gomes, G.; Pollice, R.; Aspuru-Guzik, A., Navigating through the Maze of Homogeneous Catalyst Design with Machine Learning. *Trends in Chemistry* **2021**, *3* (2), 96-110.

83. Li, X.; Chiong, R.; Page, A. J., Group and Period-Based Representations for Improved Machine Learning Prediction of Heterogeneous Alloy Catalysts. *J. Phys. Chem. Lett.* **2021**, *12* (21), 5156-5162.
84. Janet, J. P.; Ramesh, S.; Duan, C.; Kulik, H. J., Accurate Multiobjective Design in a Space of Millions of Transition Metal Complexes with Neural-Network-Driven Efficient Global Optimization. *ACS Cent. Sci.* **2020**, *6* (4), 513-524.
85. Janet, J. P.; Kulik, H. J., Resolving Transition Metal Chemical Space: Feature Selection for Machine Learning and Structure–Property Relationships. *J. Phys. Chem. A* **2017**, *121* (46), 8939-8954.
86. Janet, J. P.; Liu, F.; Nandy, A.; Duan, C.; Yang, T.; Lin, S.; Kulik, H. J., Designing in the Face of Uncertainty: Exploiting Electronic Structure and Machine Learning Models for Discovery in Inorganic Chemistry. *Inorg. Chem.* **2019**, *58*, 10592-10606.
87. Janet, J. P.; Gani, T. Z. H.; Steeves, A. H.; Ioannidis, E. I.; Kulik, H. J., Leveraging Cheminformatics Strategies for Inorganic Discovery: Application to Redox Potential Design. *Ind. Eng. Chem. Res.* **2017**, *56* (17), 4898-4910.
88. Nandy, A.; Duan, C.; Janet, J. P.; Gugler, S.; Kulik, H. J., Strategies and Software for Machine Learning Accelerated Discovery in Transition Metal Chemistry. *Industrial & Engineering Chemistry Research* **2018**, *57* (42), 13973-13986.
89. Li, Z.; Omidvar, N.; Chin, W. S.; Robb, E.; Morris, A.; Achenie, L.; Xin, H., Machine-Learning Energy Gaps of Porphyrins with Molecular Graph Representations. *J. Phys. Chem. A* **2018**, *122* (18), 4571-4578.
90. Häse, F.; Roch, L. M.; Kreisbeck, C.; Aspuru-Guzik, A., Phoenix: A Bayesian Optimizer for Chemistry. *ACS Cent. Sci.* **2018**, *4* (9), 1134-1145.
91. Okamoto, Y., Applying Bayesian Approach to Combinatorial Problem in Chemistry. *J. Phys. Chem. A* **2017**, *121* (17), 3299-3304.
92. Gubaev, K.; Podryabinkin, E. V.; Shapeev, A. V., Machine Learning of Molecular Properties: Locality and Active Learning. *J. Chem. Phys.* **2018**, *148* (24), 241727.
93. Li, Z.; Wang, S.; Xin, H., Toward Artificial Intelligence in Catalysis. *Nat. Catal.* **2018**, *1* (9), 641-642.
94. Friederich, P.; Häse, F.; Proppe, J.; Aspuru-Guzik, A., Machine-Learned Potentials for Next-Generation Matter Simulations. *Nat. Mater.* **2021**, *20* (6), 750-761.
95. Smith, J. S.; Nebgen, B.; Lubbers, N.; Isayev, O.; Roitberg, A. E., Less is More: Sampling Chemical Space with Active Learning. *J. Chem. Phys.* **2018**, *148* (24), 241733.
96. Yuan, R.; Liu, Z.; Balachandran, P. V.; Xue, D.; Zhou, Y.; Ding, X.; Sun, J.; Xue, D.; Lookman, T., Accelerated Discovery of Large Electrostrains in BaTiO₃-Based Piezoelectrics Using Active Learning. *Advanced Materials* **2018**, *30* (7), 1702884.
97. Janet, J. P.; Duan, C.; Yang, T.; Nandy, A.; Kulik, H., A Quantitative Uncertainty Metric Controls Error in Neural Network-Driven Chemical Discovery. *Chem. Sci.* **2019**, *10*, 7913-7922.
98. del Rosario, Z.; Rupp, M.; Kim, Y.; Antono, E.; Ling, J., Assessing the Frontier: Active Learning, Model Accuracy, and Multi-Objective Candidate Discovery and Optimization. *J. Chem. Phys.* **2020**, *153* (2), 024112.
99. Bradford, E.; Schweidtmann, A. M.; Lapkin, A., Efficient Multiobjective Optimization Employing Gaussian Processes, Spectral Sampling and a Genetic Algorithm. *Journal of Global Optimization* **2018**, *71* (2), 407-438.

100. Keane, A. J., Statistical Improvement Criteria for Use in Multiobjective Design Optimization. *AIAA Journal* **2006**, *44* (4), 879-891.
101. Groves, J. T.; McClusky, G. A., Aliphatic Hydroxylation via Oxygen Rebound. Oxygen Transfer Catalyzed by Iron. *J. Am. Chem. Soc.* **1976**, *98* (3), 859-861.
102. Vennelakanti, V.; Nandy, A.; Kulik, H. J., The Effect of Hartree-Fock Exchange on Scaling Relations and Reaction Energetics for C–H Activation Catalysts. *Topics in Catalysis* **2021**.
103. Winkler, J. R.; Gray, H. B., Electronic Structures of Oxo-Metal Ions. In *Molecular Electronic Structures of Transition Metal Complexes I. Structure and Bonding*, Mingos, D.; Day, P.; Dahl, J., Eds. Springer, Berlin: Heidelberg, 2011; Vol. 142, pp 17-28.
104. Liao, P.; Getman, R. B.; Snurr, R. Q., Optimizing Open Iron Sites in Metal–Organic Frameworks for Ethane Oxidation: A First-Principles Study. *ACS Appl. Mater. Interfaces* **2017**, *9*, 33484-33492.
105. Cho, K.; Leeladee, P.; McGown, A. J.; DeBeer, S.; Goldberg, D. P., A High-Valent Iron–Oxo Corrolazine Activates C–H Bonds via Hydrogen-Atom Transfer. *J. Am. Chem. Soc.* **2012**, *134* (17), 7392-7399.
106. Andrikopoulos, P. C.; Michel, C.; Chouzier, S.; Sautet, P., In Silico Screening of Iron-Oxo Catalysts for CH Bond Cleavage. *ACS Catal.* **2015**, *5* (4), 2490-2499.
107. Wang, V. C.-C.; Maji, S.; Chen, P. P.-Y.; Lee, H. K.; Yu, S. S.-F.; Chan, S. I., Alkane Oxidation: Methane Monooxygenases, Related Enzymes, and Their Biomimetics. *Chem. Rev.* **2017**, *117* (13), 8574-8621.
108. Costas, M.; Chen, K.; Que, L., Biomimetic Nonheme Iron Catalysts for Alkane Hydroxylation. *Coord. Chem. Rev.* **2000**, *200-202*, 517-544.
109. Kim, I. Y.; de Weck, O. L., Adaptive Weighted Sum Method for Multiobjective Optimization: a New Method for Pareto Front Generation. *Structural and Multidisciplinary Optimization* **2005**, *31* (2), 105-116.
110. Matano, Y.; Imahori, H., Phosphole-Containing Calixpyrroles, Calixphyrins, and Porphyrins: Synthesis and Coordination Chemistry. *Acc. Chem. Res.* **2009**, *42* (8), 1193-1204.
111. Matano, Y.; Miyajima, T.; Ochi, N.; Nakabuchi, T.; Shiro, M.; Nakao, Y.; Sakaki, S.; Imahori, H., Syntheses, Structures, and Coordination Chemistry of Phosphole-Containing Hybrid Calixphyrins: Promising Macrocyclic P,N₂X-Mixed Donor Ligands for Designing Reactive Transition-Metal Complexes. *J. Am. Chem. Soc.* **2007**, *130* (3), 990-1002.
112. Groom, C. R.; Bruno, I. J.; Lightfoot, M. P.; Ward, S. C., The Cambridge Structural Database. *Acta Crystallographica Section B Structural Science, Crystal Engineering and Materials* **2016**, *72* (2), 171-179.
113. Jones, D. R.; Schonlau, M.; Welch, W. J., Efficient Global Optimization of Expensive Black-Box Functions. *Journal of Global Optimization* **1998**, *13* (4), 455-492.
114. Welch, B. L., The Significance of the Difference Between Two Means when the Population Variances are Unequal. *Biometrika* **1938**, *29* (3/4), 350.
115. Baglia, R. A.; Zaragoza, J. P. T.; Goldberg, D. P., Biomimetic Reactivity of Oxygen-Derived Manganese and Iron Porphyrinoid Complexes. *Chem. Rev.* **2017**, *117* (21), 13320-13352.
116. Schneider, J. E.; Goetz, M. K.; Anderson, J. S., Statistical Analysis of C–H Activation by Oxo Complexes Supports Diverse Thermodynamic Control Over Reactivity. *Chem. Sci.* **2021**, *12* (11), 4173-4183.

117. Kozuch, S.; Shaik, S., How to Conceptualize Catalytic Cycles? The Energetic Span Model. *Acc. Chem. Res.* **2010**, *44* (2), 101-110.
118. Gani, T. Z. H.; Kulik, H. J., Unifying Exchange Sensitivity in Transition Metal Spin-State Ordering and Catalysis Through Bond Valence Metrics *J. Chem. Theory Comput.* **2017**, *13*, 5443-5457.
119. Petachem. TeraChem. <http://www.petachem.com> (accessed May 17, 2019).
120. Becke, A. D., Density-Functional Thermochemistry. III. The Role of Exact Exchange. *J. Chem. Phys.* **1993**, *98* (7), 5648-5652.
121. Lee, C.; Yang, W.; Parr, R. G., Development of the Colle-Salvetti Correlation-Energy Formula into a Functional of the Electron Density. *Phys. Rev. B* **1988**, *37*, 785-789.
122. Stephens, P. J.; Devlin, F. J.; Chabalowski, C. F.; Frisch, M. J., Ab Initio Calculation of Vibrational Absorption and Circular Dichroism Spectra Using Density Functional Force Fields. *J. Phys. Chem.* **1994**, *98* (45), 11623-11627.
123. Grimme, S.; Antony, J.; Ehrlich, S.; Krieg, H., A Consistent and Accurate Ab Initio Parametrization of Density Functional Dispersion Correction (DFT-D) for the 94 Elements H-Pu. *J. Chem. Phys.* **2010**, *132* (15), 154104.
124. Becke, A. D.; Johnson, E. R., A Density-Functional Model of the Dispersion Interaction. *J. Chem. Phys.* **2005**, *123* (15), 154101.
125. Wadt, W. R.; Hay, P. J., Ab Initio Effective Core Potentials for Molecular Calculations. Potentials for Main Group Elements Na to Bi. *J. Chem. Phys.* **1985**, *82* (1), 284-298.
126. Hay, P. J.; Wadt, W. R., Ab Initio Effective Core Potentials for Molecular Calculations. Potentials for the Transition Metal Atoms Sc to Hg. *J. Chem. Phys.* **1985**, *82* (1), 270-283.
127. Rassolov, V. A.; Pople, J. A.; Ratner, M. A.; Windus, T. L., 6-31G* Basis Set for Atoms K through Zn. *J. Chem. Phys.* **1998**, *109* (4), 1223-1229.
128. Saunders, V. R.; Hillier, I. H., A "Level-Shifting" Method for Converging Closed Shell Hartree-Fock Wave Functions. *Int. J. Quantum Chem.* **1973**, *7* (4), 699-705.
129. Wang, L.-P.; Song, C., Geometry Optimization Made Simple with Translation and Rotation Coordinates. *J. Chem. Phys.* **2016**, *144* (21), 214108.
130. Ioannidis, E. I.; Gani, T. Z. H.; Kulik, H. J., molSimplify: A Toolkit for Automating Discovery in Inorganic Chemistry. *J. Comput. Chem.* **2016**, *37*, 2106-2117.
131. O'Boyle, N. M.; Banck, M.; James, C. A.; Morley, C.; Vandermeersch, T.; Hutchison, G. R., Open Babel: An Open Chemical Toolbox. *J. Cheminf.* **2011**, *3*, 33.
132. O'Boyle, N. M.; Morley, C.; Hutchison, G. R., Pybel: a Python Wrapper for the OpenBabel Cheminformatics Toolkit. *Chem. Cent. J.* **2008**, *2*, 5.
133. RDKit. <http://www.rdkit.org> (accessed March 2020).
134. Prakash, J.; Sheng, Y.; Draksharapu, A.; Klein, J. E. M. N.; Cramer, C. J.; Que, L., Facile Conversion of syn-[Fe^{IV}(O)(TMC)]²⁺ into the anti Isomer via Meunier's Oxo-Hydroxo Tautomerism Mechanism. *Angew. Chem., Int. Ed.* **2019**, *58* (7), 1995-1999.
135. Wilson, S. A.; Chen, J.; Hong, S.; Lee, Y.-M.; Clémancey, M.; Garcia-Serres, R.; Nomura, T.; Ogura, T.; Latour, J.-M.; Hedman, B.; Hodgson, K. O.; Nam, W.; Solomon, E. I., [Fe^{IV}=O(TBC)(CH₃CN)]²⁺: Comparative Reactivity of Iron(IV)-Oxo Species with Constrained Equatorial Cyclam Ligation. *J. Am. Chem. Soc.* **2012**, *134* (28), 11791-11806.
136. Ray, K.; England, J.; Fiedler, A. T.; Martinho, M.; Münck, E.; Que, L., An Inverted and More Oxidizing Isomer of [Fe^{IV}(O)(tmc)(NCCH₃)]²⁺. *Angewandte Chemie* **2008**, *120* (42), 8188-8191.

137. Duan, C.; Janet, J. P.; Liu, F.; Nandy, A.; Kulik, H. J., Learning from Failure: Predicting Electronic Structure Calculation Outcomes with Machine Learning Models. *J. Chem. Theory Comput.* **2019**, *15* (4), 2331-2345.
138. Duan, C.; Liu, F.; Nandy, A.; Kulik, H. J., Putting Density Functional Theory to the Test in Machine-Learning-Accelerated Materials Discovery. *J. Phys. Chem. Lett.* **2021**, *12* (19), 4628-4637.
139. Henkelman, G.; Uberuaga, B. P.; Jónsson, H., A Climbing Image Nudged Elastic Band Method for Finding Saddle Points and Minimum Energy Paths. *J. Chem. Phys.* **2000**, *113* (22), 9901-9904.
140. Henkelman, G.; Jónsson, H., Improved Tangent Estimate in the Nudged Elastic Band Method for Finding Minimum Energy Paths and Saddle Points. *J. Chem. Phys.* **2000**, *113* (22), 9978-9985.
141. Ufimtsev, I. S.; Martinez, T. J., Quantum Chemistry on Graphical Processing Units. 3. Analytical Energy Gradients, Geometry Optimization, and First Principles Molecular Dynamics. *J. Chem. Theory Comput.* **2009**, *5* (10), 2619-2628.
142. Kästner, J.; Carr, J. M.; Keal, T. W.; Thiel, W.; Wander, A.; Sherwood, P., DL-FIND: An Open-Source Geometry Optimizer for Atomistic Simulations. *J. Phys. Chem. A* **2009**, *113* (43), 11856-11865.

TOC Graphic

